Soft Matter

PAPER

View Article Online
View Journal

Cite this: DOI: 10.1039/d1sm01237a

The effect of grain shape and material on the nonlocal rheology of dense granular flows†

Farnaz Fazelpour, * Zhu Tang * and Karen E. Daniels

Nonlocal rheologies allow for the modeling of granular flows from the creeping to intermediate flow regimes, using a small number of parameters. In this paper, we report on experiments testing how particle properties affect the model parameters used in the Kamrin & Koval cooperative nonlocal model, using particles of three different shapes (circles, ellipses, and pentagons) and three different materials, including one which allows for the measurement of stresses *via* photoelasticity. Our experiments are performed on a quasi-2D annular shear cell with a rotating inner wall and a fixed outer wall. Each type of particle is found to exhibit flows which are well-fit by nonlocal rheology, with each particle having a distinct triad of the local, nonlocal, and frictional parameters. While the local parameter b is always approximately unity, the nonlocal parameter A depends sensitively on both the particle shape and material. The critical stress ratio μ_s, above which Coulomb failure occurs, varies for particles with the same material but different shape, indicating that geometric friction can dominate over material friction.

Received 25th August 2021,
Accepted 18th January 2022

DOI: 10.1039/d1sm01237a

rsc.li/soft-matter-journal

1 Introduction

While idealized studies of granular materials most commonly use circular-shaped particles, these do not correspond to the majority of granular materials present in industrial and geophysical applications. In this paper, we examine the effect of particle properties on the rheology of granular flows, both experimentally and by fitting to a nonlocal model which has previously been validated only for circular particles.[1–5] Similar to what has been done for local rheological modeling of faster flows,[6–10] it is necessary to determine which aspects of the constitutive laws are affected by various particle properties.

The study of the rheology of granular materials is based on quantifying the relationship between the stress applied to the material, and the resulting flow. We use the dimensionless inertial number I to describe the speed of the flow:[11]

$$I \equiv \frac{\dot{\gamma} d}{\sqrt{P/\rho}}. \quad (1)$$

This represents the ratio between a microscopic time for rearrangements $T = d/\sqrt{P/\rho}$ (under pressure P pushing a particle of diameter d and density ρ into a hole) and a macroscopic timescale $1/\dot{\gamma}$, which is the mean deformation time under shear rate $\dot{\gamma}$. Large values of I correspond to rapid flow, while small values are slow, even creeping. In this paper, we focus on 2D experiments in the regime $10^{-7} < I < 10^{-4}$, where it is possible to both individually-track particles and to measure the boundary stresses;[5] for some particles, we also obtain stress measurement within the bulk, through the use of photoelasticity.[12,13] The loading stress is characterized by the nondimensional ratio between the shear stress τ and the pressure P:

$$\mu \equiv \frac{\tau}{P}. \quad (2)$$

In a local rheology, there is no flow at locations where μ is less than a yield criterion μ_s. However, for slow flows, it has been observed that this criterion fails to explain a number of experimental results such as a transition from solid-like to liquid-like behavior,[14] shear or vibration in one region fluidizing a distant region,[15,16] or the dependence of the shear bandwidth on geometry and grain size.[17,18] The recent development of nonlocal rheologies[1,2,4,19–21] aims to provide predictive models which correctly account for the observation of flows where $\mu < \mu_s$. We have previously observed that two of these nonlocal models (the cooperative model by Kamrin and Koval,[1] and the gradient model by Bouzid *et al.*[19]) are able to provide this predictive power in a 2D granular rheometer[5] over a variety of packing fractions and flow rates.

In this paper, we directly test the dependence of the nonlocal rheological parameters on particle stiffness and particle shape. For our experiments, we compare particles of three different shapes (circles, ellipses, pentagons) and three different elastic moduli. The choice of these three shapes allows us to test for the effects of particle anisotropy (circles *vs.* ellipses) and particle angularity (circles *vs.* pentagons). Angular particles are

Department of Physics, North Carolina State University, Raleigh, NC, USA.
E-mail: kdaniel@ncsu.edu

† Electronic supplementary information (ESI) available. See DOI: 10.1039/d1sm01237a

particularly interesting because there are two types of contacts: side–side and side–vertex (vertex–vertex contacts are rare). We identify that having angular *vs.* rounded particle shape strongly modifies the yield criterion, while particle shape and modulus jointly control the length scale of the nonlocal effects.

1.1 The cooperative model

The Kamrin & Koval cooperative model is a nonlocal rheological model[1,2,4] which has been developed to overcome the shortcomings of local rheology mentioned above. It is a phenomenological model that extends a local Bagnold-like granular flow rule to include additional nonlocal effects. This model has been tested for steady state flows, using both experiments (2D systems)[5] and simulations (2D and 3D systems).[1,2,22] In this paper, we use a 2D geometry, allowing us to perform both particle-tracking and local stress measurements: pressure $P(r)$ and shear stress $\tau(r)$.

In a local rheology, the inertial number I and the stress ratio μ have a linear relationship wherever μ is larger than the yield criterion μ_s.[23] Thus, the local rheology $I(\mu)$ relationship is described using the Heaviside function H:

$$I(\mu) = \frac{(\mu - \mu_s)H(\mu - \mu_s)}{b} \tag{3}$$

where there is no flow for $\mu < \mu_s$. The parameter b is a constant which models the steepness of the $I(\mu)$ relationship. The cooperative model starts from the Bagnold flow rule specifying that the shear stress and shear rate have a linear relationship. Motivated by this relationship, the fluidity is defined as:

$$g \equiv \frac{\dot{\gamma}}{\mu} \tag{4}$$

where the stress ratio μ is defined in eqn (2) and g has the same units as the shear rate $\dot{\gamma}$ (s^{-1}).

The fluidity g arises from two contributions. One is from local rheology, denoted g_{loc}, and takes into account only local variables: $\dot{\gamma}$ in eqn (4) is calculated from eqn (1) and (3). By substitution, the local fluidity is given by:

$$g_{loc}(\mu, P) = \frac{(\mu - \mu_s)H(\mu - \mu_s)}{b\mu T}. \tag{5}$$

The total fluidity g arises from nonlocal effects diffusing from other regions. This is modeled by a Laplacian term, scaled by a length scale ξ which sets the length scale of this influence:

$$\nabla^2 g = \frac{1}{\xi^2}(g - g_{loc}). \tag{6}$$

The length scale ξ is measured in units of the particle diameter d, and takes the form:

$$\frac{\xi}{d} = A\sqrt{\frac{1}{|\mu - \mu_s|}}. \tag{7}$$

where A is a constant depending on the particle properties, and controls the spatial extent of the nonlocal effects. The length scale $\xi(\mu)$ is symmetric around $\mu = \mu_s$, and the system is most sensitive to small perturbations near the yield ratio μ_s.

Because we are working in a 2D system, we chose for simplicity to decompose the stress tensor into the (scalar) shear and normal stresses. For the tensorial form of this nonlocal model, see papers by Kamrin and coworkers.[1–3]

2 Method

2.1 Apparatus

Our experiments are performed on a quasi-2D annular shear cell with a rotating inner wall (R_i = 15 cm) and a fixed outer wall (R_o = 28 cm). A motor (Parker Compumotor BE231FJ-NLCN with a PV90FB 50 : 1 gearbox) is attached to the inner wall, providing a constant rotational speed. We measure the inner wall shear stress $\tau(R_i)$ *via* a torque sensor (Cooper Instruments & Systems) attached to the central shaft. As shown in Fig. 1, the stationary outer wall incorporates 52 laser-cut leaf springs. Each of the springs linearly deforms (both radially and tangentially) under stress from the granular material. *Via* calibrated image processing,[24] we obtain quantitative measurements of shear (τ) and normal (P) stresses at each of the 52 spring tips. All values below are reported as spatial and temporal averages, and all experiments were performed by rotating the inner wall with a speed v = 1.1 cm s^{-1}. We collect all data after several full

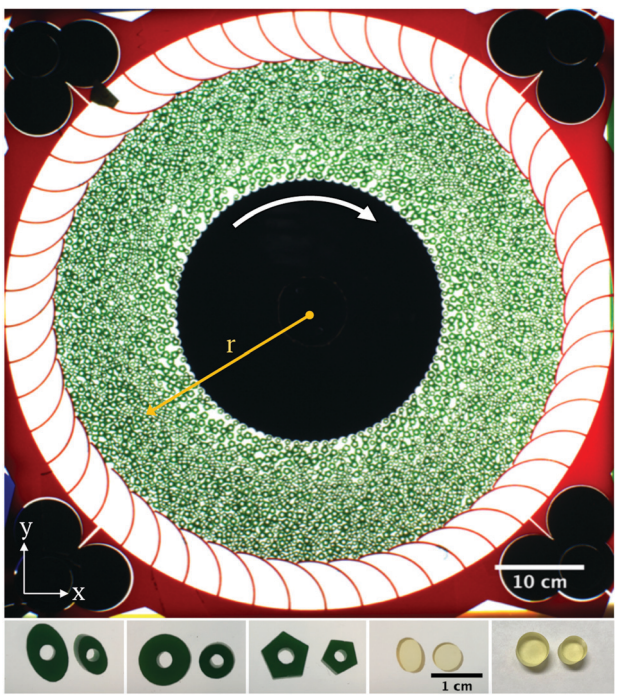

Fig. 1 Top: Top view of annular Couette experiment filled with flat pentagonal particles. The inner wheel rotates at a constant speed $v(R_i)$, the coordinate r measures the distance from the center of inner wheel, and gravity acts into the page. Bottom: Photos of the three stiffest acrylic (Ac) shapes: ellipses, circles, and pentagons, along with the circular/elliptical particles (Vi3), and the softest circular photoelastic particles (Vi4). The central holes allow for easier particle-tracking. Each of the acrylic particles can be circumscribed by a square of side length 0.7 cm (small particles) or 1.0 cm (large particles).

rotations of the inner wall, to ensure that we have achieved steady state.

We use three types of particles in these experiments. The particles for testing shape-dependence are cut from 3 mm thick acrylic (bulk modulus 3 GPa and density $\rho = 1.14$ g cm^{-3}); these are referred to as Ac in the figure legends. As shown in Fig. 1, the particles are laser-cut with holes at their centers to aid in particle-tracking. The dimensions of the bidisperse particles were selected to have a size ratio of $\sqrt{2}$ to suppress both crystallization and segregation and thereby achieve steady state flows without developing size-gradients or patchy domains. The circles have diameters $d_L = 1.0$ cm and $d_S = 0.7$ cm. The ellipses have (minor, major) axes (0.81 cm, 1.21 cm) and (0.57 cm, 0.85 cm), with d defined as the geometric mean of the major and minor axes, selected to match the same values as the circles. The pentagons have side lengths of 0.65 cm (large) and 0.46 cm (small), so that for d taken to be the distance from one side to the opposite vertex these also match the same values as for the circles. In all cases, the ratio of large to small particle is 1 : 2 by number, corresponding to approximately equal areas for the two components.

For testing the effects of material stiffness, we added two additional particle types. First, the particles used in Tang *et al.*:[5] these are a bidisperse mixture of circular (60%) and elliptical (40%) disks cut from 3 mm thick PhotoStress Plus PS-3 polymer from the Vishay Measurements Group (bulk modulus 0.21 GPa and density $\rho = 1.15$ g cm^{-3}), these are referred to as Vi3. Second, the particles used in Owens and Daniels:[25,26] these are a bidisperse mixture of $d_S = 0.9$ cm and $d_L = 1.1$ cm circles in equal concentrations, cut from 6.35 mm thick Vishay PhotoStress material PSM-4 (bulk modulus $E = 4$ MPa and density $\rho = 1.06$ g cm^{-3}), these are referred to as Vi4. Because Vi4 is made of a soft photoelastic material, it allows for the visualization of internal forces, as shown in Fig. 2. By solving an inverse problem on the fringe pattern within each disk, we measure the vector force at each contact, resulting in knowing the shear ($\tau(r)$) and normal ($P(r)$) stresses throughout the material. Details about this process are available in.[12,13,27–29] Unlike for the other particles (Ac and Vi3) where we measure τ and P only at the boundaries (torque sensor and leaf spring calibration), the Vi4 photoelastic particles provide a more quantitative validation of the nonlocal rheology.

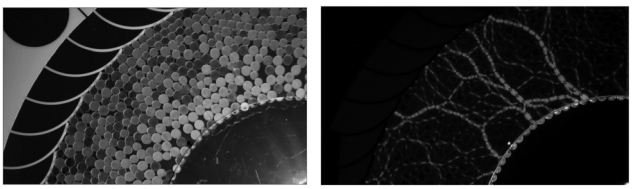

Fig. 2 Sample image of Vi4 particles under shear. Left: Image of particles illuminated by non-polarized (red) light, for particle-tracking. Right: Image of particles illuminated by polarized (green) light, for measuring the internal forces *via* photoelastimetry. See the ESI,† for a video of the dynamics of such force chains under white light.

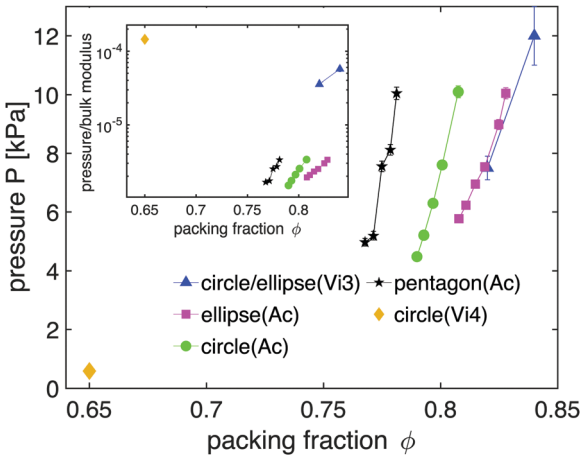

Fig. 3 Experimentally-determined relationship between the packing fraction ϕ and the pressure P for different particle types, all sheared at an inner wall rotation rate of $v(R_i) = 1.1$ cm s^{-1}. In the legend, Vi3 represents particles cut from Vishay PS-3 (data from Tang *et al.*[5]), Vi4 represents particles cut from Vishay PSM-4, and Ac represents particles cut from acrylic. The pressure is measured either by taking the time-average of the normal stress measured for all of the 52 spring tips (Ac and Vi3 particles), or by taking the time- and particle-average of the normal stress measured from photoelasticity (Vi4 particles). The error bars represent standard error. The inset shows the relationship between the ratio of pressure to bulk modulus of each particle set and packing fraction ϕ.

For all experiments, the outer wall and a single layer of particles rest upon a glass substrate; the effects due to basal friction between the particles and the substrate are described in Section 2.3 below. The Vi4 particles are not confined by an upper surface, the Ac and Vi3 are, but in all cases they primarily form persistent contacts with their neighbors in the plane.

Importantly, different particle shapes have dramatically-different packing densities. Random close packing (RCP) for discs,[30] ellipses,[31] and pentagons[32] are 0.84, 0.895, and 0.80, respectively. In order to conduct experiments at approximately constant pressure, we mapped out the relationship between packing fraction ϕ and the measured pressure P for runs at consistent rotation rate. This data is shown in Fig. 3; for our rheological measurements, we selected a value of ϕ to achieve one of two values of pressure: $P = 7.5$ kPa and $P = 10.0$ kPa. Experiments at the larger pressure probe both the local and nonlocal flow regimes, while experiments at the lower pressure are nonlocal throughout. Since the Vi4 particles are several orders of magnitude softer than the other particles, we performed their experiments at a lower pressure ($P = 0.58$ kPa). In Fig. 3, we plot the pressure as a function of packing fraction to illustrate the choice of ϕ. The inset shows the same data rescaled by the bulk modulus of each particle set, to aid in comparing across several orders of magnitude.

A summary of all experimental runs is provided in Table 1, including measurements of the shear stress at the inner wall. Note that we observe that runs with a higher packing fraction ϕ (also higher pressure P) have a higher inner wall shear stress S_0. Each experiment's microscopic timescale T is calculated from the associated pressure measurement P, together with particle

Table 1 Summary of the datasets. The inner wall rotation speed $v(R_i)$ is set by the motor controller. The number of particles is set by hand to provide the target pressure. The microscopic timescale T is calculated based on measured P and the known values of d and ρ. The Vi3 column contains data from Tang *et al.*[5]

Material	Acrylic (Ac)	Acrylic (Ac)	Acrylic (Ac)	Acrylic (Ac)	Acrylic (Ac)	Acrylic (Ac)	Vishay PS-3 (Vi3)	Vishay PSM-4 (Vi4)
Shape	Ellipses	Ellipses	Circles	Circles	Pentagons	Pentagons	Circles/ellipses	Circles
$v(R_i)$ [d s^{-1}]	1.3	1.3	1.3	1.3	1.3	1.3	2	1.1
# Of particles	3242	3210	2920	2895	3438	3426	5610	1724
P [kPa]	10 ± 0.2	7.5 ± 0.1	10 ± 0.2	7.5 ± 0.1	10 ± 0.2	7.5 ± 0.1	7.5 ± 0.4	0.58 ± 0.02
S_0 [kPa]	3.5 ± 0.6	1.4 ± 0.3	2.9 ± 0.5	1.6 ± 0.3	2.2 ± 0.4	1.5 ± 0.3	0.8 ± 0.2	0.18 ± 0.04
T [ms]	2.9 ± 0.1	3.3 ± 0.1	2.9 ± 0.1	3.3 ± 0.1	2.9 ± 0.1	3.3 ± 0.1	2.2 ± 0.1	13.5 ± 0.1

properties; all are approximately 3 ms, except for Vi4 which has a timescale several times larger due to the lower pressure.

2.2 Measuring speed and shear rate

We locate the centroids of the particles using Matlab's Hough transform,[33] and create space-time trajectories using the Blair-Dufresne particle-tracking algorithm.[34] The tangential speed profile $v(r)$ is calculated within concentric rings of width $0.5d$. To calculate the shear rate, we use Fourier-derivatives as described in Tang *et al.*[5] Note that, due to the annular geometry, the shear rate is given by $\dot{\gamma}(r) = \frac{1}{2}\left(\frac{\partial v}{\partial r} - \frac{v}{r}\right)$. These measurements are presented in Fig. 4, analyzed from 10^4 frames for each dataset. We observe that for circular and elliptical particles, the runs at lower P have smaller values of v and $\dot{\gamma}$ when compared at the same distance from the inner wall. Pentagonal particles do not exhibit this dependence.

2.3 Estimating basal friction effects

As previously reported in Tang *et al.*,[5] it is necessary to account for the basal friction in order to correctly measure the local shear stress on each particle. For those particles for which we do not have photoelastic force measurements (Ac and Vi3), we assume that the stress from the basal friction is proportional to the local packing fraction ϕ. We calculate $\phi(r)$ for each particle type using the coarse-graining method of Weinhart *et al.*,[35] based on the tracked locations of all particles. For the Lucy function used for coarse-graining, we find that a width parameter of w = 1.3 is sufficient to remove major fluctuations without being over-smoothed. As shown in Fig. 5, the data can be approximated by an exponential with a decay parameter r_0. We fit each curve to the equation

$$\phi(r) = \phi_0[1 - e^{-\Delta r/r_0}] + \phi(R_i) \quad (8)$$

where the parameter $\phi_0 \equiv \phi(R_o) - \phi(R_i)$ is the difference in packing fraction between the outer wall and the inner wall and $\Delta r = r - R_i$ is the distance from the inner wall. We observe that mixtures containing elliptical particles pack the most densely, followed by circular particles and then pentagons, as also observed in Fig. 3.

Using eqn (8), we write a phenomenological model for the shear stress:

$$\tau(r) = S_0\left(\frac{R_i}{r}\right)^2 + \tau_0\left[1 - e^{-\Delta r/r_0}\right] \quad (9)$$

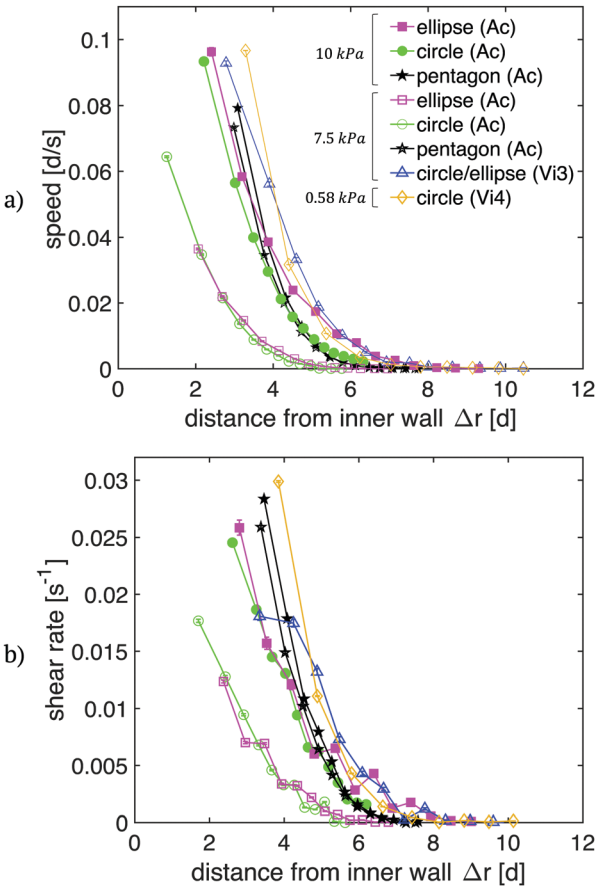

Fig. 4 (a) Tangential speed profile $v(r)$ and (b) shear rate $\dot{\gamma}(r)$, measured using particle tracking and plotted as a function of distance $\Delta r = r - R_i$ from inner wall. Vi3 data is reproduced from Tang *et al.*[5] Error bars are the standard error.

This model consists of two parts. The first term arises from the annular geometry, with the parameter S_0 corresponding to the torque measured at the central shaft. The second term arises from the forces due to basal friction, with the parameter r_0 taken from the fits to the packing fraction curves shown in Fig. 5.

For the Ac and Vi3 particles, the parameter τ_0 is calculated from $\tau(R_o) - S_0\left(\frac{R_i}{r}\right)^2$ with $\tau(R_o)$ measured from the leaf springs. This is a semi-empirical result that is interpolated between the inner and outer walls (symbols in Fig. 6). We

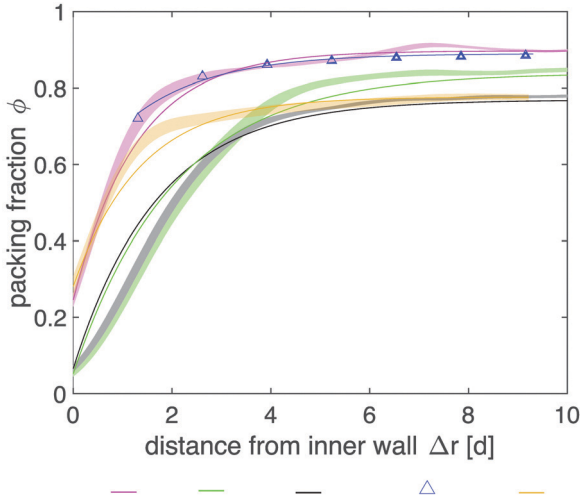

	Ellipses (Ac)	Circles (Ac)	Pentagons (Ac)	Circle/Ellipse (Vi3)	Circles (Vi4)
r_0	1.28	2.04	1.69	1.67	1.36
τ_0 [Pa]	180	200	160	250	1.28

Fig. 5 The local packing fraction for different particle shapes and materials at P = 7.5 kPa (P = 0.58 kPa for Vi4 particles), calculated *via* coarse-graining. The error bars are the standard error, and the solid curves are the corresponding fits to eqn (8). The circle/ellipse (Vi3) data are from Tang *et al.*[5] The table shows the fitting parameters from eqn (8) and (9) for each particle shape and material. These parameters are taken to be constant for the same particles, independent of pressure.

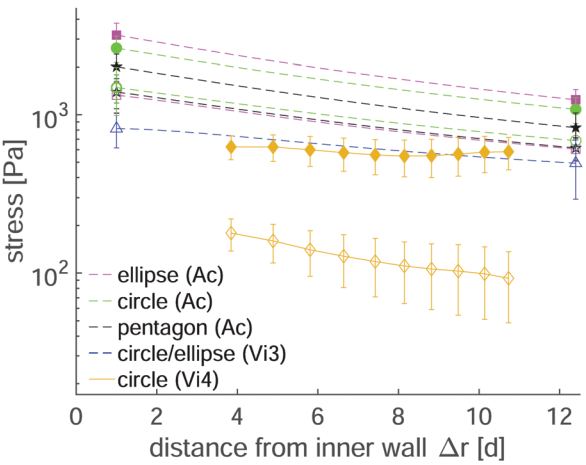

Fig. 6 Stress profiles for all types of particles. Dashed-lines are shear stress for Ac and Vi3 particles obtained from eqn (9), using boundary measurements only. Filled symbols are taken at P = 10 kPa and open symbols are taken at P = 7.5 kPa, with matching symbol and line colors. Solid lines are the photoelastically-measured pressure (solid diamonds) and shear stress (open diamonds) for the Vi4 particles. The error bars are spatial and temporal standard deviations.

measure the full shear stress profiles using eqn (9) (dashed-lines in Fig. 6), and the pressure $P(r)$ is assumed to be constant throughout the material $P = \langle P(r) \rangle$. For both the high and low pressure datasets taken for the same particle shape, we use the same set of (r_0, τ_0) parameters since the difference in particle number is only about 1%. These values are given in the table within Fig. 5.

For the Vi4 particles, we perform photoelastic stress measurements on 2000 frames (taken at 0.2 Hz, see sample image in Fig. 2) and time-average the coarse-grained stress field calculated from the vector contact forces. This provides the shear stress $\tau(r)$ and pressure $P(r)$ throughout the material, as shown in Fig. 6. For this dataset, the parameters in eqn (9) can be found with S_0 and τ_0 obtained directly from fitting shear stress profiles, and r_0 obtained from packing fraction fit (Fig. 5). In this case, we measure all stresses directly rather than relying on eqn (9).

These different methods of measurements have advantages and disadvantages. For instance, the boundary stress measurements (for Ac and Vi3 particles) gives stress values directly at the inner and outer wall, but we cannot measure stress directly all throughout material. The photoelasticity method (Vi4) measures stress throughout the material, but falls short of the inner and outer walls due to lighting imperfections and the coarse-graining length scale.

3 Results

The comparison that follows utilizes the cooperative model of Kamrin and Kova1,[1] using methods previously described in Tang *et al.*[5] In Fig. 7a, we plot the experimentally-measured $\mu(I)$ relationships for all three particle materials and all three particle shapes. Note that in all cases, the low-P run lies at lower μ than the high-P run for the same particles shape, which arises because the shear stress τ decreases even faster than P. For example, for the runs using elliptical particles, the inner wall stress $\tau(R_i)$ drops from 3500 Pa to 1400 Pa, for only a 25% decrease in pressure.

In all cases, we are able to fit the experimentally-determined $\mu(I)$ data using the cooperative model, using the parameters listed in Table 2. The next sections describe the fitting techniques used to obtain these results.

3.1 Rheological parameters

For the seven datasets taken for Ac and Vi3 particles, we performed the same particle-tracking and boundary stress measurements as done in Tang *et al.*[5] For the Vi4 dataset, we perform the same particle-tracking, but the stress measurements are done using photoelasticity (see Fig. 2). To measure the yield stress ratio μ_s, we performed an additional run (not shown in Table 1) at $v(R_i) = 0.0013d$ s^{-1}, for which we previously observed that the ratio of the inner wall shear stress to the pressure is a good estimate.[5] These values are shown in Table 2. We observed that all circular/elliptical particles have a similar value of μ_s, while the angular particles yield at a much lower stress ratio. This reflects that the shape of the interparticle contacts (rounded *vs.* angular) is an important control on μ_s, beyond material properties such as coefficient of friction or elastic modulus.[36]

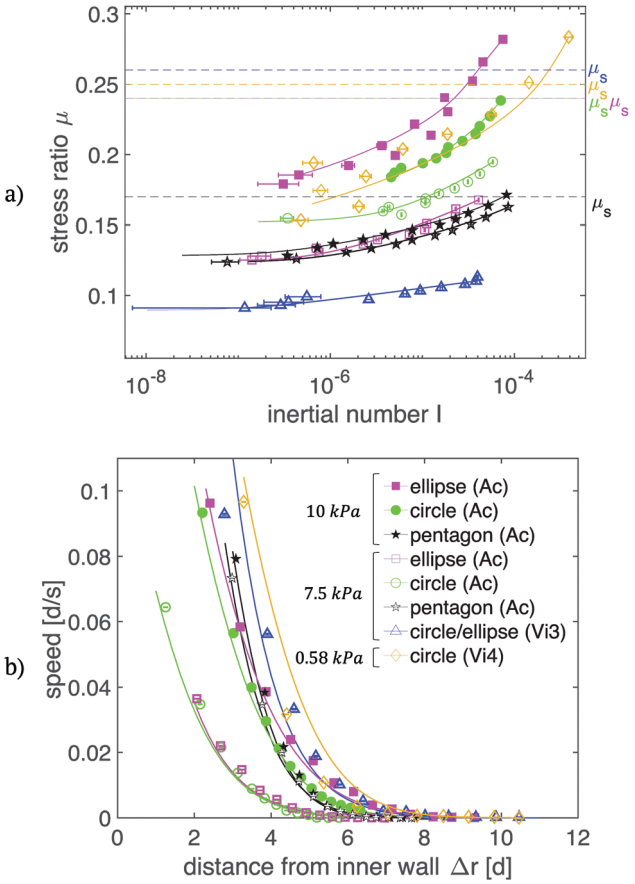

Fig. 7 (a) Stress ratio μ, obtained from eqn (2), as a function of inertial number I, for all eight datasets, both measured locally using binned (velocity) or coarse-grained (stress) data. The horizontal dashed-lines indicate the measured critical stress ratio μ_s for each particle type. (b) Speed profiles $v(r)$ for all eight datasets. In both plots, the symbols are the measured data, with the cooperative model (see Section 1.1, using model parameters from Table 2) shown by the solid curves. The error bars in both plots are the standard errors measured in the experimental results.

For each dataset, we find the fluidity profile $g(r)$ by solving eqn (6) using the Matlab ODE solver. We set the boundary conditions empirically, by measuring g near the wall. To obtain values for parameters (A, b), we use Levenberg–Marquardt optimization to fit the $g(r)$ dataset for each particle type. For the Ac particles, we measure the parameters (A, b) at $P = 10$ kPa, and then apply these same parameters to the dataset collected at $P = 7.5$ kPa. The resulting parameters are shown in Table 2, and the best fitting curves are shown in Fig. 7. We observe that values of the nonlocal parameter A are similar (but not identical) for rounded particles with the same material, but differ for pentagonal particles. The pentagonal particles have a smaller nonlocal parameter A, indicative of a weaker nonlocal effect (shorter nonlocal diffusion lengthscale ξ). This observation is consistent with the experimental results of Kozlowski *et al.*,[37] where the spatial extent of the force chains was observed to be shorter for pentagonal particles than disks. The particle material plays an important role in determining the nonlocal parameter A: rounded particles of different material have different nonlocal parameters. Values of the local parameter b are insensitive to the particle properties, whether material or shape.

3.2 Length scale

The lengthscale ξ in eqn (7) represents the influence of the nonlocal term in the vicinity of μ_s. To check this dependence and the effects of particle shape on it independently, we pick three different particle shapes all cut from acrylic (at pressure $P = 10$ kPa), to determine whether the assumptions of the model are justified. The measured lengthscale is calculated by eqn (6) using the analytical method presented in Tang *et al.*,[5] and the theoretical curves are calculated by eqn (7).

To perform this validation, we perform an empirical fit to the speed profile $v(r)$, in order to take the necessary higher-order derivatives. We (as previously given in Tang *et al.*[5]) observe that the empirical speed profile function is well-fit by

$$v(r) = v_0 \exp[\alpha_3 r^3 + \alpha_2 r^2 + \alpha_1 r + \alpha_0]. \quad (10)$$

The resulting fits in the vicinity of μ_s are shown in Fig. 8. Note that $v(r)$ for the circular particles fails to fall off as quickly as was observed for the elliptical and pentagonal particles. In the original movies obtained for these experiments, we confirm this observation, and additionally observe that the run with circular particles exhibits significant crystallization effects. Because crystallized domains are more stable under higher pressure than lower pressure,[38] they are more efficient at transmitting shear at larger distances from the shearing surface. Since the calculation of ξ does not take place in this outer region, we are able to proceed with the model validation.

From eqn (7), we expect a divergence of $\xi(\mu)$ at μ_s, and the kinematics of the particles thereby provides an independent measurement of μ_s. We estimate its location by drawing an arbitrary horizontal line in Fig. 8(b), and determining the two intersection points of this horizontal line and the $\xi^2(\mu)$ curve. The measured value of μ_s lies at the mean ξ of these two intersections: for circular particles $\mu_s = 0.23$, for elliptical particles, $\mu_s = 0.22$, and for pentagonal particles, $\mu_s = 0.16$. These values correspond closely to the values measured by quasi-static shearing, given in Table 2. Moreover, we can see

Table 2 Fit values of local and nonlocal parameters for different particle shapes and materials, with measured confidence intervals. Each column (single particle type) is valid for both measured pressures

	Acrylic ellipses	Acrylic circles	Acrylic pentagons	Vishay PS-3 circles/ellipses	Vishay PSM-4 circles
μ_s	0.24 ± 0.02	0.24 ± 0.02	0.17 ± 0.01	0.26 ± 0.01	0.25 ± 0.01
b	1.1 ± 0.5	1.1 ± 0.5	1.1 ± 0.5	1.1 ± 0.5	1.1 ± 0.5
A	0.28 ± 0.01	0.30 ± 0.02	0.13 ± 0.02	0.41 ± 0.02	0.22 ± 0.03

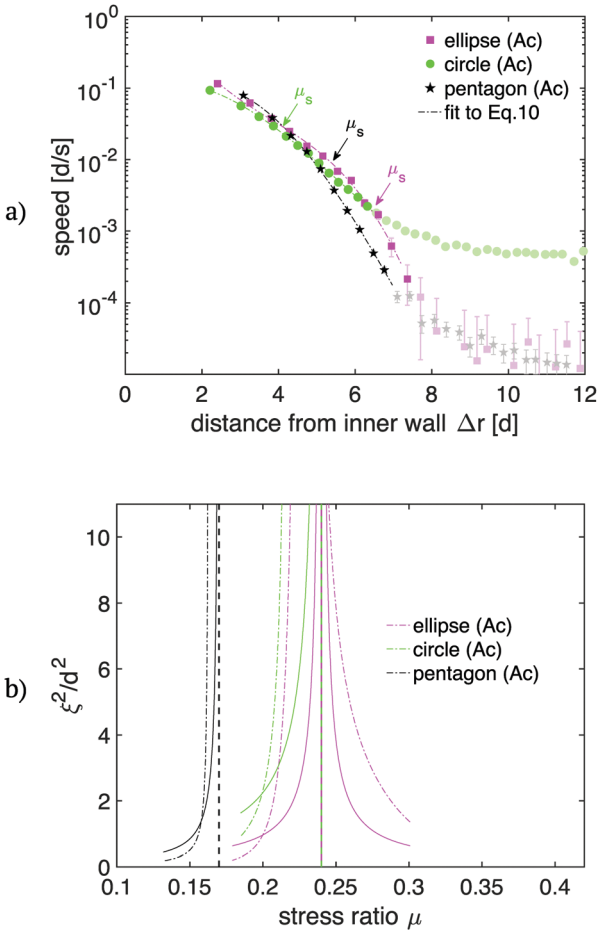

Fig. 8 (a) Speed profile for P = 10 kPa datasets, for particles with different shapes. Only the brighter data points (in the vicinity of μ_s) are used for fitting eqn (10) (dash-dotted curves), with the dimmer data points shown for completeness. (b) Comparison of measured length scale (the dash-dotted curves) to the theoretical curves (solid curves). The particle shapes are given by the same colors as in (a).

variations in the nonlocal effects for different particle shapes in Fig. 8(b) where $\xi^2(\mu)$ takes a wider form in circular/elliptical particles than pentagons.

4 Microscopic description of granular fluidity

According to a recent interpretation[4] of the granular fluidity g, the only variables affecting the granular fluidity g are the velocity fluctuation δv (the square root of the granular temperature) and the packing fraction ϕ. This motivates writing the granular fluidity g in a microscopic form:

$$g = \frac{\delta v}{d} F(\phi). \tag{11}$$

While the physical origin of the function $F(\phi)$ remains unknown, simulation results from Zhang and Kamrin[4] showed that the function $F(\phi)$ is independent of the driving speed and

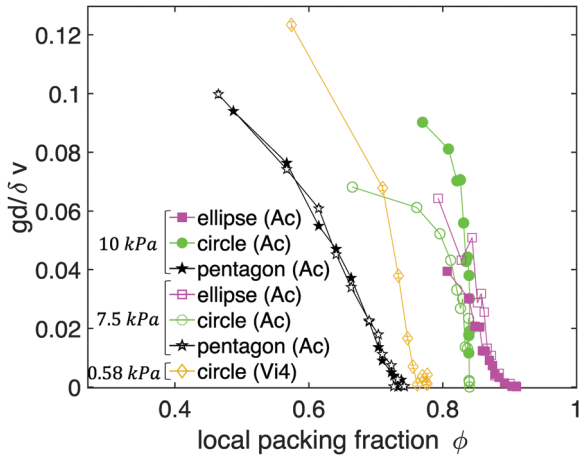

Fig. 9 Determination of the function $F(\phi)$ from eqn (11), for different Ac shapes (both pressures) and Vi4 (lower pressure). Data are experimentally-determined from the same bins as used in the $\mu(I)$ plot shown in Fig. 7a. The error bars are from the standard error of granular fluidity g.

experiment geometry, and depends only on the packing fraction ϕ and the particle properties.

We test this definition using particles of different shape but the same material (acrylic) and same shape (circles) but different material. Here, we exclude the Vi3 particles since the mixture of ellipses and circles does not have a clear comparison in the other datasets. The velocity fluctuations are measured within concentric rings of width $0.5d$, using the same data presented in Fig. 4. As shown in Fig. 9, the shape of the particles affects the function $F(\phi)$: each shape and material has its own characteristic curve that ends at ϕ_{RCP} for that specific shape/material. While the elliptical and pentagonal particles display a consistent shape, independent of pressure, the circular particles do not. Instead, the shape of $F(\phi)$ changes, likely due to the wall-crystallization observations presented earlier.

5 Conclusions

We have established the success of the cooperative nonlocal model[1–4] in describing the rheology of non-circular particles. The particle shape and modulus both play an important role in the particular choice of modeling parameters. We reported the relationship between particle properties and nonlocal effects. While the local parameter b is independent of the particle shape or material, the critical stress ratio μ_s only depends on the particle shape and not the particle material, and the nonlocal parameter A is strongly sensitive to both the particle shape and stiffness. Nonlocal effects are observed to be more important for rounded particles than for angular particles, as measured by the magnitude of A. For similar shapes, we observe that softer particles have very different nonlocal effects set by the softness of the particles. Among all 3 model parameters, the nonlocal parameter A is the most sensitive to grain properties, both shape and material. To obtain these parameters (A, b), we set the boundary conditions from empirical

observations and see that the results are sensitive to the choice of boundary condition. The open question is how we can set the boundary conditions from first principles, and what role the walls play in these results. Finally, we find that the particle-scale definition of granular fluidity takes a similar shape to that observed in simulations,[4] and may be strongly affected by crystallization.

Conflicts of interest

There are no conflicts to declare.

Acknowledgements

We thank Michael Shearer and Theodore Brzinski for useful discussions about the project, and Austin Reid for inspiring the boundary wall designs. We are grateful to the National Science Foundation (NSF DMR-1206808 and DMS-1517291) for the construction of the particles and apparatus, and the International Fine Particle Research Institute (IFPRI) for financial support.

Notes and references

1 K. Kamrin and G. Koval, *Phys. Rev. Lett.*, 2012, **108**, 178301.
2 D. L. Henann and K. Kamrin, *Proc. Natl. Acad. Sci. U. S. A.*, 2013, **110**, 6730–6735.
3 K. Kamrin and D. L. Henann, *Soft Matter*, 2015, **11**, 179–185.
4 Q. Zhang and K. Kamrin, *Phys. Rev. Lett.*, 2017, **118**, 058001.
5 Z. Tang, T. A. Brzinski, M. Shearer and K. E. Daniels, *Soft Matter*, 2018, **14**, 3040–3048.
6 E. Azéma, F. Radja, R. Peyroux and G. Saussine, *Traffic and Granular Flow'07*, Springer, 2009, pp. 497–505.
7 E. Azéma, F. Radja and J.-N. Roux, *Eur. Phys. J. E: Soft Matter Biol. Phys.*, 2018, **41**, 2.
8 E. Azéma, Y. Descantes, N. Roquet, J.-N. Roux and F. Chevoir, *Phys. Rev. E: Stat., Nonlinear, Soft Matter Phys.*, 2012, **86**, 031303.
9 E. Azéma, F. Radjai and G. Saussine, *Mech. Mater.*, 2009, **41**, 729–741.
10 B. Saint-Cyr, J.-Y. Delenne, C. Voivret, F. Radjai and P. Sornay, *Phys. Rev. E: Stat., Nonlinear, Soft Matter Phys.*, 2011, **84**, 041302.
11 Y. Forterre and O. Pouliquen, *Annu. Rev. Fluid Mech.*, 2008, **40**, 1–24.
12 K. E. Daniels, J. E. Kollmer and J. G. Puckett, *Rev. Sci. Instrum.*, 2017, **88**, 051808.
13 A. Abed Zadeh, J. Bares, T. A. Brzinski, K. E. Daniels, J. Dijksman, N. Docquier, H. O. Everitt, J. E. Kollmer, O. Lantsoght, D. Wang, M. Workamp, Y. Zhao and H. Zheng, *Granular Matter*, 2019, **21**, 83.
14 G. Koval, J.-N. Roux, A. Corfdir and F. Chevoir, *Phys. Rev. E: Stat., Nonlinear, Soft Matter Phys.*, 2009, **79**, 021306.
15 K. Nichol, A. Zanin, R. Bastien, E. Wandersman and M. van Hecke, *Phys. Rev. Lett.*, 2010, **104**, 078302.
16 K. Reddy, Y. Forterre and O. Pouliquen, *Phys. Rev. Lett.*, 2011, **106**, 108301.
17 G. MiDi, *Eur. Phys. J. E: Soft Matter Biol. Phys.*, 2004, **14**, 341–365.
18 X. Cheng, J. B. Lechman, A. Fernandez-barbero, G. S. Grest, H. M. Jaeger, G. S. Karczmar, M. E. Mobius and S. R. Nagel, *Phys. Rev. Lett.*, 2006, **96**, 38001.
19 M. Bouzid, M. Trulsson, P. Claudin, E. Clément and B. Andreotti, *Phys. Rev. Lett.*, 2013, **111**, 238301.
20 M. Bouzid, A. Izzet, M. Trulsson, E. Clément, P. Claudin and B. Andreotti, *Eur. Phys. J. E: Soft Matter Biol. Phys.*, 2015, **38**, 125.
21 P. V. Dsouza and P. R. Nott, *J. Fluid Mech.*, 2020, **888**, R3.
22 K. Kamrin and G. Koval, *Comput. Part. Mech.*, 2014, **1**, 169–176.
23 F. Da Cruz, S. Emam, M. Prochnow, J.-N. Roux and F. Chevoir, *Phys. Rev. E: Stat., Nonlinear, Soft Matter Phys.*, 2005, **72**, 021309.
24 Z. Tang, T. A. Brzinski and K. E. Daniels, *EPJ Web Conf.*, 2017, **140**, 03035.
25 E. T. Owens and K. E. Daniels, *Soft Matter*, 2013, **9**, 1214–1219.
26 E. T. Owens and K. E. Daniels, *Europhys. Lett.*, 2011, **94**, 54005.
27 J. E. Kollmer, *Photo-Elastic Granular Solver (PEGS)*, 2019, https://github.com/jekollmer/PEGS.
28 K. Liu, J. E. Kollmer, K. E. Daniels, J. Schwarz and S. Henkes, *Phys. Rev. Lett.*, 2021, **126**, 088002.
29 F. Fazelpour and K. E. Daniels, *EPJ Web Conf.*, 2021, **249**, 03014.
30 C. Voivret, F. Radjai, J.-Y. Delenne and M. S. El Youssoufi, *Phys. Rev. E: Stat., Nonlinear, Soft Matter Phys.*, 2007, **76**, 021301.
31 G. Delaney, D. Weaire, S. Hutzler and S. Murphy, *Philos. Mag. Lett.*, 2005, **85**, 89–96.
32 C. Wang, K. Dong and A. Yu, *Phys. Rev. E: Stat., Nonlinear, Soft Matter Phys.*, 2015, **92**, 062203.
33 *Hough Transform*, https://www.mathworks.com/help/images/ref/imfindcircles.html.
34 D. Blair and E. Dufresne, The Matlab Particle Tracking Code Repository, http://site.physics.georgetown.edu/matlab/.
35 T. Weinhart, R. Hartkamp, A. R. Thornton and S. Luding, *Phys. Fluids*, 2013, **25**, 070605.
36 S. Papanikolaou, C. S. O'Hern and M. D. Shattuck, *Phys. Rev. Lett.*, 2013, **110**, 198002.
37 R. Kozlowski, H. Zheng, K. E. Daniels and J. E. S. Socolar, *Soft Matter*, 2021, **17**, 10120–10127.
38 E. Khain and B. Meerson, *Phys. Rev. E: Stat., Nonlinear, Soft Matter Phys.*, 2006, **73**, 061301.

